Journal of Materials Chemistry A

Accepted Manuscript

ROYAL SOCIETY OF CHEMISTRY

www.rsc.org/materialsA

Journal of Materials Chemistry A

RSCPublishing

ARTICLE

Novel 3DOM $BiVO_4/TiO_2$ Nanocomposites for Highly Enhanced Photocatalytic Activity

Cite this: DOI: 10.1039/x0xx00000x

Received 00th January 2012,
Accepted 00th January 2012

DOI: 10.1039/x0xx00000x

www.rsc.org/

Meryam Zalfani,[+ab] Benoit Van der Schueren,[+a] Zhi-Yi Hu,[+c] Joanna C. Rooke,[a] Ramzi Bourguiga,[b] Min Wu,*[d] Yu Li,*[d] Gustaff Van Tendeloo,[c] and Bao-Lian Su*[ade]

Novel 3DOM $BiVO_4/TiO_2$ nanocomposites with intimate contact were for the first time synthesized by a hydrothermal method in order to elucidate their visible-light-driven photocatalytic performances. $BiVO_4$ nanoparticles and 3DOM TiO_2 inverse opal have been fabricated respectively. These materials were characterized by XRD, XPS, SEM, TEM, N_2 adsorption-desorption and UV-vis diffuse (UV-vis) and photoluminescence spectroscopies. As references for comparison, a physical mixture of $BiVO_4$ nanoparticles and 3DOM TiO_2 inverse opal powder (0.08:1) and a $BiVO_4$/P25 TiO_2 (0.08:1) nanocomposite made also by hydrothermal method have been prepared. The photocatalytic performance of all the prepared materials was evaluated by the degradation of Rhodamine B (RhB) as model pollutant molecule under visible light irradiation. The highly ordered 3D macroporous inverse opal structure can provide more active surface areas and increased mass transfer because of its highly accessible 3D porosity. The results show that 3DOM $BiVO_4/TiO_2$ nanocomposites possess a highly prolonged life time and increased separation of visible light generated charges and extraordinarily high photocatalytic activity. Owing to the intimate contact between $BiVO_4$ and large surface area 3DOM TiO_2, the photogenerated high energy charges can be easily transferred from $BiVO_4$ to 3DOM TiO_2 support. $BiVO_4$ nanoparticles in 3DOM TiO_2 inverse opal structure act thus as a sensitizer to absorb visible light and to transfer efficiently high energy electrons to TiO_2 to keep photogenerated charges long life and well separated, owing to its direct band gap of 2.4 eV, favourably positioned band edges, very low recombination rate of electron-hole pairs and stability when coupled with photocatalysts, explaining the extraordinarily high photocatalytic performance of 3DOM $BiVO_4/TiO_2$ nanocomposites. It is found that more $BiVO_4$ in nanocomposite, longer time the photogenerated charge separation and higher phtocatalytic activity. This work can shed light on the development of novel visible light responsive nanomaterials for efficient solar energy utilisation by the intimate combination of an inorganic light sensitizing nanoparticle with inverse opal structure with high diffusion efficiency and high accessible surface area.

1. Introduction

In recent years, semiconductor photocatalysts have attracted a great deal of attention due to their potential application in environmental remediation. Among these semiconductors, TiO_2 has been extensively investigated as the most promising photocatalyst because of its safety, low-cost and high efficiency under UV light irradiation.[1] However, the broad band gap energy of this metal oxide limits its use in visible light[2] as TiO_2 is active only under ultraviolet (UV) light, about 3–5% of the solar spectrum. In addition, low rate of electron transfer to oxygen and a high recombination rate of photo generated electron–hole pairs result in its low photo quantum efficiency.[3-5] Many strategies have been developed to improve photocatalytic efficiency of TiO_2 through the second component doping to promote the photon to electron conversion efficiency, the photogenerated charge separation and the visible light harvesting. The combination of TiO_2 with a sensitizer semiconductor system has shown superior performance such as enhanced or tuneable light absorption within TiO_2, improved photo-generated electron-hole separation and exalted interfacial charge transfer efficiency.[6] Coupling narrow-band-gap semiconductors such as CdS,[7] $CuBi_2O_4$,[8] with wide band-gap semiconductors like TiO_2, SnO_2[9] and WO_3,[10] and forming composite photocatalysts such as Bi_2WO_6/TiO_2, Bi_2O_3/TiO_2, In_2O_3/TiO_2, Cu_2O/TiO_2, WO_3/TiO_2, etc., have been extensively investigated.[11-15] Keet al.[16] showed that the WO_3/TiO_2 nanocomposites present much higher photocatalytic activity than pure TiO_2 in the photodegradation reaction of Rhodamine B (RhB) under UV light. Vinodgopal et al.[17] studied a coupled SnO_2/TiO_2 semiconductor system which carried out a very rapid and complete decolorization of the textile azo dye under UV irradiation. Bessekhouad et al.[18] reported that Bi_2O_3/TiO_2 heterojunction structure presented higher activity than pure Bi_2O_3 and TiO_2-P25 for the photocatalytic degradation of Orange II under UV–vis irradiation.

The monoclinic $BiVO_4$ structure was reported to show highly promising photocatalytic activity under visible light irradiation due to

its relatively narrow band gap energy of 2.4 eV, compared to its two tetragonal phases both with band gap energy of 3.1 eV.[19-21] Due to its visible light photocatalytic activity, it has also been used for the degradation of organic pollutants and oxygen evolution in the water splitting reaction.[22-23] The combination of the narrow band gap semiconductor material as $BiVO_4$ with TiO_2 to produce $BiVO_4/TiO_2$ nanocomposite with intimate heterojunction could be an efficient way to offer a visible light photocatalyst with high photocatalytic activity and attracts increasing attention.[20,24-30] Cao et al.[24] synthesized the porous peanut-like $BiVO_4/TiO_2$ composite nanostructures by hydrothermal process and the photocatalytic activity of these $BiVO_4/TiO_2$ nanostructures was largely enhanced. Zhang et al.[25] reported the synthesis of $BiVO_4/TiO_2$ by a one-step microwave hydrothermal method, and found that the 20 wt % $TiO_2/BiVO_4$ nanocomposite exhibits the better photocatalytic activity compared to pure monoclinic $BiVO_4$ and other percentages of TiO_2 in $BiVO_4$ because of its high crystallinity, narrow band gap, and most importantly, the hierarchical heterostructure which can effectively separate photoinduced electron–hole pairs on the surface of $BiVO_4/TiO_2$ photocatalysts. They claimed that $BiVO_4$ played a role of light sensitizer. The sensitizer effect of $BiVO_4$ has also been pointed out by Tang et al.[30] Colon et al [20,31] studied ternary erbium doped $BiVO_4/TiO_2$ heterostructure made by a simple impregnation method which showed highly enhanced photocatalytic activity in the degradation of phenol[20] and methylene blue[31]. They attributed this high photocatalytic activity of erbium doped $BiVO_4/TiO_2$ to the occurrence of a luminescence process generated by erbium ions and the possibility to adjust the band position between Er^{3+} doped $BiVO_4$ and TiO_2, leading to the effective charge pair separation. Hu et al[26] prepared $BiVO_4/TiO_2$ with a mass ratio of 1:200 by hydrothermal treatment for benzene degradation reaction and claimed that their material was 3-4 times more active than nitrogen doped TiO_2 under visible light irradiation. A bilayer TiO_2 photonic crystal (PC)/porous $BiVO_4$ was constructed by using liquid-phase deposition and Spin coating by Hou et al [32]. The photocatalytic ability of porous $BiVO_4$ was enhanced by combination with a TiO_2 PC layer as the back reflector which intensified the light absorbance, showing another advantage of a TiO_2 PC crystal in enhancing light absorption and the comination of $BiVO_4$ and TiO_2. In spite of these promising results, the role of $BiVO_4$ in $BiVO_4/TiO_2$ heterostructures and photoelectronic mechanism remain a point in debate. Moreover, the accessibility of reactants to these heterostructures is not favourable due to the low porosity, low surface area of TiO_2 supports and low adsorptive properties of $BiVO_4$.[21,33] Xie et al [29] in their recent paper showed very clearly the importance of combination of TiO_2 and $BiVO_4$ to achieve long life visible light excited charge carriers which gave unexpectedly high photocatalytic activity for water splitting. Pure Mo doped $BiVO_4$ inverse opal structures have been prepared. [34] Due to the specific structure, the higher photocurrent density owing to the effective charge collection was observed leading to an enhancement in photoelectrochemical water splitting and showing the importance of macroporous inverse opal structure in charge collection.

The photocatalytic behaviour of highly ordered three dimensional macroporous titania with an inverse opal structure and good accessibility of reactants in dye molecule degradation has been investigated.[35-40] Wu et al.[35] studied the degradation of RhB with 3DOM TiO_2 inverse opal structure with different pore diameters. They have shown that the photocatalytic activity presents a variation with the pore diameter. In this framework, Zheng et al.[36] demonstrated that the order of Benzoic acid (BA), Methyl Orang (MO) and RhB photocatalytic degradation is related with pore size of the TiO_2 inverse opal structure (IOS). With the increasing of the pore size of the TiO_2 IOS, the mass transfer and light utilization efficiency are enhanced. The continuous pore voids facilitate the transfer of reactant molecules which is beneficial for dye sensitization.

On the other side, since 3DOM inverse opal structures as photonic crystals (PC) have periodic dielectric contrast modulation in the length scale of the wavelength of light, coherent Bragg diffraction forbids light with certain energies to propagate through the material along a particular crystallographic direction. This gives rise to stop-band reflection, and the range of energies that is reflected back depends on the periodicity and dielectric contrast of the PC. At the wavelengths corresponding to the edges of these stop-bands, photons propagate with strongly reduced group velocity; hence called 'slow photons'. The slow photons can be used to enhance the light absorption of materials when the photon energy matches the absorbance of the material leading to the generation of a large number of electron-hole pairs and an enhanced photocatalytic activity. Liu et al.[38-40] investigated the slow photon effect on the photocatalytic activity of inverse opal ZnO by tuning the incident light angle.[38-40] Compared with bulk ZnO, it was found that inverse opal ZnO exhibits much higher photocatalytic activity.

Chen et al.[41] have also demonstrated that inverse opal WO_3 photoanodes with different stop-bands showed an enhanced photocurrent intensity. Photonic crystals, particularly titania, have been considered as components in dye-sensitized photoelectrochemical cells designed to increase the efficiency of the solar cells by enhancing photocurrent efficiencies due to the localization of heavy photons near the edges of photonic gaps.[42-46] The slow photon effect on photovoltaic cells and photochemical process was investigated by Nishimura et al.[46] and Chen et al.[47-49] as a means of promoting the optical absorbance of TiO_2 based composite system. In addition to this slow photon effect, 3DOM structure has an open interconnected porous network, facilitating the diffusion of molecules and offering a larger surface area, both being quite favourable for photocatalysis.[50, 51]

In order to benefit from the advantages of both the composite system and the 3DOM structure, we have combined the 3DOM TiO_2 with narrow band gap semiconductor $BiVO_4$ as a light sensitizer leading to the visible light absorbing materials with enhanced photocatalytic activity. To the best of our knowledge, we have for the first time prepared 3DOM $BiVO_4/TiO_2$ nanocomposites offering a heterojunction by their intimate contact. In this work, the synthesis, characterization, and photocatalytic activity of 3DOM $BiVO_4/TiO_2$ nanocomposites in the visible light degradation of a dye molecular model were studied. The mechanism of enhanced visible light photocatalytic activity of the as-synthesized nanocomposites is proposed and discussed. For comparison, TiO_2 inverse opal, $BiVO_4$ nanoparticles, a physical mixture of $BiVO_4$ nanoparticles and 3DOM TiO_2 powders, and $BiVO_4$/P25 TiO_2 nanocomposite by hydrothermal method were synthesized and used as references.

2. Experimental

2.1 Synthesis of 3DOM TiO_2, $BiVO_4$ and 3DOM TiO_2-$BiVO_4$nanocomposites

Styrene, sodium hydroxide and potassium persulfate were purchased from Aldrich. Polystyrene (PS) spheres were synthesized by an emulsion polymerization method without the addition of surfactant. The styrene (20 mL) was washed three times with a solution of NaOH (1M) to remove the polymerization inhibitor, and then added to 160 mL of bidistilled water in a two-neck flask. This solution was stirred at 350 rpm under an inert atmosphere and heated to 70 °C. After 30 min and when the temperature was stabilised at 70 °C, 0.16 g of $K_2S_2O_8$ was added to initiate polymerization. After 30 min the mixture become cloudy and after 6 hours the polymerization was stopped by cooling and venting the flask. The white solution obtained

was a dispersion of PS beads in water. The PS sphere size is around 350 nm.

To obtain an opal structured template, the PS beads dispersion was self-assembled by oven-drying at 40°C for 5 days and characterised by scanning electron microscopy.

The fabrication of three dimensionally ordered macroporous (3DOM) titania was achieved via a templating strategy, as reported in the literature,[35,38-40,52,53] in which a thick layer of self-assembled polystyrene spheres (PS) were deposited onto a filter paper in a Buchner funnel under vacuum. The PS assembly was then infiltrated with the precursor solution. Titanium isopropoxide (Aldrich, 97%) was added dropwise to completely cover the PS spheres whilst under vacuum such that it occupied the voids inside the PS assembly. The precursor-template mixture was then air dried for 24 h and subsequently calcined at 550 °C for 12 h at a heating rate of 2 °C/min to obtain TiO_2 photonic crystals (PCs) with inverse opal structure (IOS). In order to incorporate $BiVO_4$ nanoparticles inside the voids of the 3DOM TiO_2, a hydrothermal method was used. In a typical process, stoichiometric amounts of Bi $(NO_3)_3 \cdot 5H_2O$ (Carl Roth, ≥ 98%, p.a. ACS) and NH_4VO_3 (Carl Roth, ≥ 98%, p.a.) were dissolved in a stoichiometric volume of an ethylene glycol–water mixture and stirred for about 10 min until a clear solution formed. Then, different amounts of 3DOM TiO_2 were added into the solution and sonicated for 15 min. After 1h stirring, the obtained yellow-coloured mixture was transferred into a Teflon-sealed autoclave which was maintained at 160 °C for 24 h. The solid powders were recovered by centrifugation and washed with distilled water and absolute ethanol three times. Finally, the obtained solid was vacuum-dried at 60 °C for 6h, and was then calcined at 300 °C for 1h. Dumbbell-like $BiVO_4$ structures were synthesized under the same experimental conditions. Two other reference samples were prepared for photocatalytic comparison. Firstly, $BiVO_4$ nanoparticles were introduced into P25 TiO_2 nanoparticles by the same method described above by hydrothermal synthesis. After washing, the sample recovered was labelled $BiVO_4$/P25-TiO_2 nanocomposite. Secondly, the obtained $BiVO_4$ dumbbell like structure was mixed with 3DOM TiO_2 inverse opal powders, giving a physical mixture of $BiVO_4$ and 3 DOM TiO_2, labelled as phy-mix $BiVO_4$-3DOM TiO_2 IO.

2.2 Material characterisation

Powder X-ray diffraction was performed on a PANalytical X'pert Pro with Cu Kα radiation. Textural properties of the materials were evaluated via adsorption-desorption of nitrogen at -196 °C using a Micromeritics Tristar 3000 with prior outgassing. The morphological properties of the samples were observed by scanning electron microscopy (SEM) (Jeol JSM-7500F) equipped with an energy dispersive X-ray detector (EDX). Furthermore, transmission electron microscopy (TEM) was performed on a Philips FEI-Tecnai 10 electron microscope with an accelerating voltage of 80 kV. X-ray photoelectron spectroscopy (XPS) analysis was performed on a K-Alpha™ + X-ray photoelectron spectrometer (XPS). The binding energy for the C (1s) peak at 284.9 eV, (relative to adventitious carbon from the XPS instrument itself), was used as a reference. The UV–Vis absorbance spectra were obtained using a UV–Vis spectrophotometer (Perkin Elmer Lambda 35 UV-visible spectrometer fitted with a Labsphere for analysis in diffuse reflectance mode) in the range of 200–750 nm. Photoluminescent properties of the samples have been studied by using Perkin Elmer LS45 Luminescence spectrometry.

2.3 Photocatalytic testing

Photocatalytic testing was performed under visible light irradiation (400-800 nm) using 6 neon lamps of 18 W. The luminous power of each lamp is 1250 lm and the total luminous power is 7500 lm in the photocatalytic reactor. The emission spectrum of Neon light lamp was given in Figure 1S. It can been seen that the intensity of UV light emitted by the neon lamp is very low and can be neglected, no UV filter has been used to cut the UV light. The reaction temperature was maintained at room temperature. In each experiment 20 mg of photocatalyst was placed in 50 mL of reactant solution with an initial concentration of 10^{-3} M of RhB. The suspension was poured into a quartz tube, inserted into a reactor and stirred in the dark for 120 min to ensure adsorption/desorption equilibrium prior to irradiation. During irradiation, 2 mL of the suspension was removed at a given time interval for subsequent RhB concentration analysis.

3. Results and discussions

3.1 Phase composition

XRD patterns of the as-prepared 3DOM TiO_2 inverse opal, two $BiVO_4$/3DOM TiO_2 nanocomposites and $BiVO_4$ nanoparticules are shown in Fig. 1. The XRD pattern (Fig. 1a) of TiO_2 inverse opal structure shows five peaks at 2θ = 25.3°, 37.9°, 48.0°, 54.6° and 62.8° corresponding to the crystal planes of (101), (004), (200), (211), and (204), respectively (JCPDS card no. 14-0688), which indicates that the TiO_2 sample adopts an anatase phase after calcination at 550 °C. The XRD peaks (Fig. 1d) of $BiVO_4$ nanoparticles correspond to the monoclinic scheelite phase (JCPDS14-0688). The diffraction profiles reveal that both $BiVO_4$ and TiO_2 powder are highly crystalline. Diffraction patterns of $BiVO_4$/3DOM TiO_2 nanocomposites (Fig. 1b and c) showed the combination of the XRD profiles of both TiO_2 inverse opal and $BiVO_4$ nanoparticles. Weak XRD diffraction peaks of vanadate species at 2θ = 18.8°, 28.8°, 30.5°, 35°, 39.9° and 42.4° corresponding to the crystal planes of (011), (121)

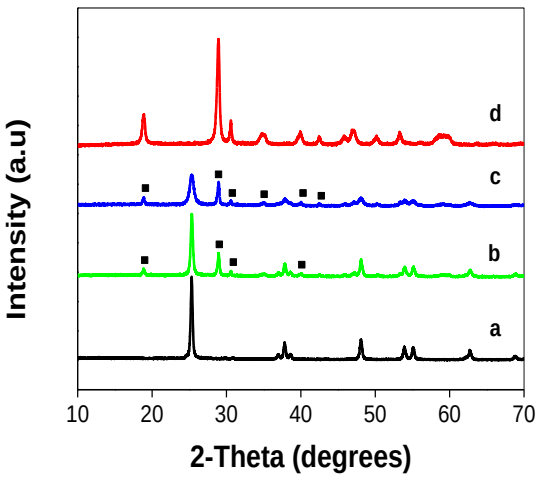

Fig. 1 X-ray diffraction patterns of (a) TiO_2 inverse opal, (b) 0.04 $BiVO_4$/3DOM TiO_2, (c) 0.08$BiVO_4$/3DOM TiO_2 nanocomposites and (d) $BiVO_4$ nanoparticles.

(040), (002), (-1,1,2) and (150), respectively, are observed as shown by (■) in Fig. 1b and c. This is presumably due to a combination of their low content and high dispersion.

The average crystallite sizes of pure $BiVO_4$ nanoparticles, pure TiO_2 inverse opal structure and TiO_2 nanoparticles in 0.08$BiVO_4$/3DOM TiO_2 nanocomposite, calculated by the Scherrer equation, were found to be 30.0, 29.4 and 22.5 nm, respectively. In general, an increase of the crystallite size is observed in the high temperature treated samples. However the TiO_2 crystallite size decreases in the $BiVO_4$/TiO_2 nanojunction composites compared to that in pure TiO_2 inverse opal, which is confirmed by the presence of broad peaks in the diffraction pattern of 0.08$BiVO_4$/3DOM TiO_2 nanocomposite.

This can be ascribed to the fact that the introduced $BiVO_4$ nanoparticles inhibits grain aggregation. With increasing content of $BiVO_4$ nanoparticles in $BiVO_4$/3DOM TiO_2, the nanoparticles of the $BiVO_4$ grew from 30 nm to about 45.2 nm, indicating nanocrystals of $BiVO_4$ shifted into the agglomerated state as a result of densification, the crystal grows.

3.2 Morphology

Fig. 2 shows SEM images of pure TiO_2 inverse opal (a and b), pure $BiVO_4$ nanoparticles (c and d) and $BiVO_4$/3DOM TiO_2 nanocomposite (e and f) respectively.

The pure macroporous TiO_2 sample exhibits (Fig. 2a and b) a highly ordered three dimensional inverse opal structure with interconnected pores. The average pore size of the TiO_2 inverse opal is about 320 nm, being smaller than that of PS spheres used (350nm) due to the contraction of inverse opal structure after removing PS spheres upon calcination.

The pure $BiVO_4$ nanoparticles (Fig. 2c) exhibit dumbbell-like shapes, highlighting that the as-prepared $BiVO_4$ product is composed of countless dumbbell-like aggregates and nearly all of them adopt the same morphology. Single dumbbell aggregated from nanoparticles has a length ranging from 1 to 5 µm. Furthermore, we can notice that the surface of the obtained $BiVO_4$ sample is fairly rough as shown in Fig. 2c, which further indicates that every dumbbell is formed by an aggregation of nanoparticles. Fig. 2d presents an enlarged SEM image of the top structure of the dumbbell (Fig. 2c). It confirms that the $BiVO_4$ is an aggregate of small sphere-like nanoparticles of 30-60 nm. Thus the dumbbell-like $BiVO_4$ is assembled by oriented aggregation nanoparticles. This morphology is quite similar to that previously reported.[21]

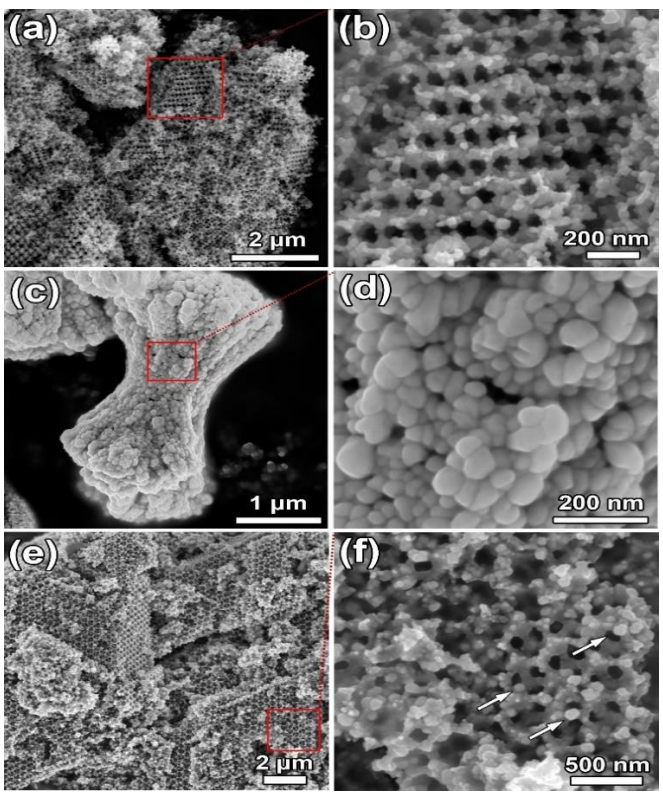

Fig. 2 SEM images, (a) and (b): inverse opal structural TiO_2 sample; (c) and (d): $BiVO_4$ sample; (e) and (f): inverse opal structural TiO_2 doping with $BiVO_4$ sample ($BiVO_4$ particles are indicated by arrows).

The SEM micrograph in Fig. 2e confirms that a $BiVO_4$/3DOM TiO_2 nanojunction was obtained. The TiO_2 inverse opal support has a highly ordered structure with few defects. In this image it can be seen that the morphology of $BiVO_4$ has changed and the particle size was greatly increased to around 45 nm (as highlighted by the arrows in Figure 2f). This is due to the effect of the calcination temperature. This observation is in very good agreement with XRD results.

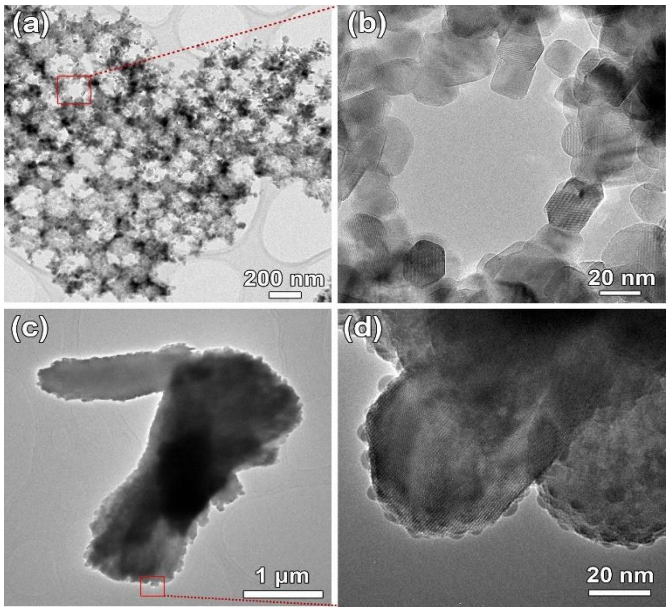

Fig. 3 TEM images, (a) and (b): inverse opal structural TiO_2 sample; (c) and (d): $BiVO_4$ Nanoparticles.

In order to get more information about the microstructure of the as-prepared products, further investigation was performed by TEM. The macrostructure of pure TiO_2 inverse opal structure was examined by TEM, where the macropores can be clearly identified in Fig. 3a via a contrast in the image between voids and material. As shown in Fig. 3b, TiO_2 is an aggregation of small nanoparticles. Fig. 3c shows a typical TEM image of dumbbell-like $BiVO_4$ nanoparticles. As can be shown in Fig. 3d, it confirms that the $BiVO_4$ is an aggregate of small nanoparticles which is in good agreement with SEM observations. The TEM, STEM images and EDX mapping of 0.08$BiVO_4$/3DOM TiO_2 nanocomposite are shown in Figure 4. The 0.08$BiVO_4$/3DOM TiO_2 nanocomposite (Fig. 4a and b) has a dual morphology with small particles corresponding to $BiVO_4$ present on the 3DOM TiO_2 structure. The bismuth vanadate adopts a new morphology (Fig. 4b) with increased size after the formation of the nanocomposite (highlighted by arrows). The elemental compositions of the $BiVO_4$/3DOM TiO_2 heterojunctions were analyzed by energy dispersive X-ray spectroscopy (EDXS). As shown in Fig. 4c-e, the EDX mapping of 0.08$BiVO_4$/3DOM TiO_2 indicated the presence of Bi, V, Ti and O atoms in the sample. Red colour showed the Ti element and green colour represented bismuth vanadate nanoparticles which are homogenously dispersed on 3DOM TiO_2 IO structure. Fig. 4e is the combination of TiO_2 and $BiVO_4$. Fig. 4 evidenced very clearly the intimate contact between 3DOM TiO_2 IO structure and $BiVO_4$ nanoparticles.

3.3 Chemical states by X-ray Photoelectron Spectroscopy (XPS)

In order to elucidate the elemental composition, the oxidation states and the chemical environment of Bi, V and Ti elements in the $BiVO_4$/TiO_2 photocatalyst, XPS analysis was performed.

Fig. 5 shows XPS spectra of the 0.08$BiVO_4$/3DOM TiO_2 nanocomposite (spectrum a), compared with pure TiO_2 inverse opal structure (spectrum b) and pure $BiVO_4$ nanoparticles (spectrum c), in different spectral regions that correspond to different elements, revealing the binding energies for Bi4f, Ti2p, V2p and O1s of the as-prepared samples.

Fig. 5d-g shows high-resolution XPS spectra of the $BiVO_4$/TiO_2 sample. As shown in spectrum d, the binding energies of Bi $4f_{7/2}$ and Bi $4f_{5/2}$ are 159.0 and 164.3 eV, respectively, indicating that this element is present as Bi (III). The binding energy values are typical for bismuth in $BiVO_4$.[51] A shift of 0.3 eV to higher binding energy in the peak positions of bismuth, as compared to pure $BiVO_4$ (158.7eV and 164.0 eV), suggesting that electron transfer from $BiVO_4$ to TiO_2 could occur, in accordance with the shift observed for bismuth. The high resolution V2p spectrum reveals a doublet with peaks centred at 524 and 516.3 eV (spectrum e), which corresponds to the $V2p_{1/2}$ orbit and $V2p_{3/2}$ orbit, respectively. These peaks also display binding energy values, typical of V (V) as reported in the literature.[51-54] Thus, the analysis of the V2p core lines of the as-prepared sample clearly indicates the presence of V^{5+} oxidation states. Compared with pure $BiVO_4$, a slightly shift for 0.3 eV is observed in the position peaks corresponding to V2p (524.0 for the V2p1/2 orbit and 516.3 eV for V2p3/2).

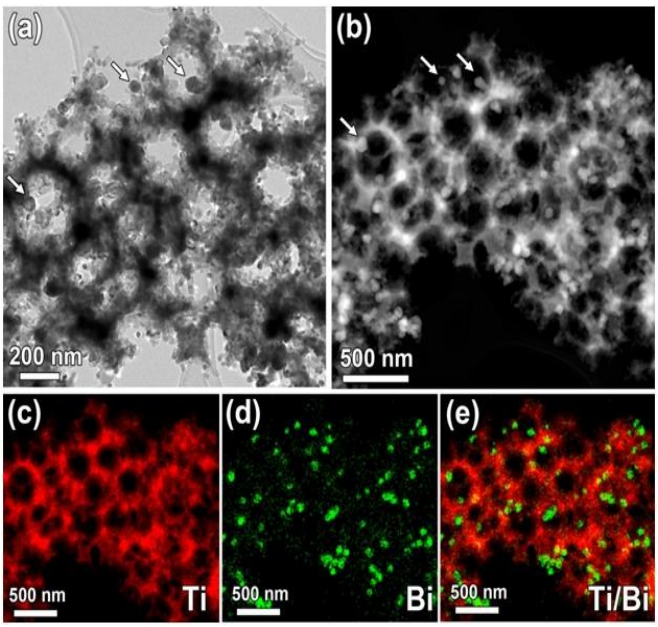

Fig.4 (a) and (b) TEM and STEM image of a same zone of inverse opal structural TiO_2 doping with $BiVO_4$ sample ($BiVO_4$ particles are indicated by arrows); (c-e) Corresponding EDX elemental mapping results.

Spectrum f depicts two bands with binding energies of 458.2 eV and 463.9 eV that are assigned to $Ti2p_{3/2}$ and $Ti2p_{1/2}$, respectively, corresponding to Ti^{4+} in a tetragonal structure such as anatase titania.[55] Compared to pure TiO_2, a shift of 0.6 eV to lower binding energy in the peak positions of TiO_2 (458.8 eV and 464.5 eV) is observed, confirming the possible charge transfer between $BiVO_4$ and TiO_2. The high-resolution XPS spectrum of the O1s (spectrum g) shows a narrow peak at a binding energy of 529.6 eV. For pure $BiVO_4$ nanoparticles and TiO_2 inverse opal structure, this peak was located at 529.4 and 530.0 eV, respectively. This asymmetric peak indicates that oxygen is present on the surface not only as lattice oxygen, but also free oxygen.[51,53,54] All of these results gave the insight that the composite was formed by TiO_2 and $BiVO_4$. Moreover, the peaks for Bi4f, V2p, Ti2p and O1s in the $BiVO_4$/3DOM TiO_2 nanocomposite had slightly shift compared with those in pure $BiVO_4$ and TiO_2 resulting from the interaction between $BiVO_4$ and TiO_2 in the composite system.

3.4 Textural Analysis

N_2 adsorption–desorption of the TiO_2 inverse opal, $BiVO_4$ and $BiVO_4$/3DOM TiO_2 nanocomposites revealed type II isotherms. For TiO_2 inverse opal, the pore size distribution plot calculated via the Barrett Joyner Halenda (BJH) method shows a narrow pore size distribution (insert Fig. 6a) centred at 2.3nm, resulting from the aggregation of TiO_2 nanoparticles. The adsorbed nitrogen volume for TiO_2 inverse opal does not reach saturation at high relative pressure p/p_o= 0.8–1.0, which indicates the presence of large macropores. Thus the N_2 isotherm obtained for TiO_2 inverse opal contains macroporosity which is from inverse opal structure. BET specific surface areas of pure $BiVO_4$ nanoparticles, pure TiO_2 inverse opal structure and $BiVO_4$/3DOM TiO_2 nanocomposites are shown in Table 1. $BiVO_4$ and TiO_2 inverse opal were found to have a surface area of 4 and 30 m^2/g, respectively. For $BiVO_4$ nanoparticles (insert of Fig. 6b), the pore size distribution is quite large. The N_2 adsorption-desorption isotherms give a hysteresis coming from the aggregation of large particles. In the case of two $BiVO_4$/3DOM TiO_2 nanocomposites (Fig. 6c and d), other than macroporosity from inverse opal structures, two pore sizes centred at 2.4 and 8 nm for 0.04$BiVO_4$/3DOM TiO_2 and 2.5 and 7 nm for 0.08$BiVO_4$/3DOM TiO_2 were observed, respectively. The pore size at 2.3-2.5 nm comes from the aggregation of TiO_2 nanoparticles whilst the pores of 7-9 nm come from the aggregation of $BiVO_4$ nanoparticles. When the amount of $BiVO_4$ nanoparticles is increased, the size of nanoparticles becomes bigger, larger pores can be formed, reducing the amount of pores of 7-9 nm. The XRD results confirmed the growth of nanoparticles with increasing $BiVO_4$ amount.

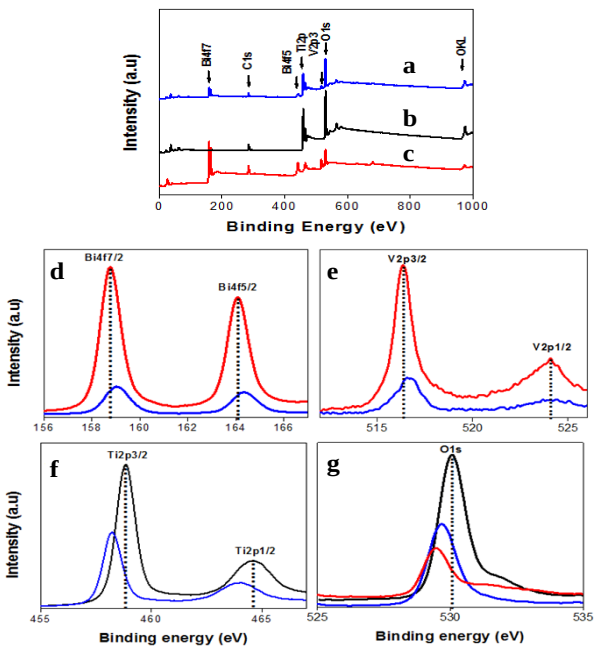

Fig. 5 Wide range XPS spectrum of the 0.08$BiVO_4$/3DOM TiO_2 nanocomposite (a), pure TiO_2 inverse opal (b) and pure $BiVO_4$ nanoparticles. High-resolution XPS spectra of Bi4f (d), V2p (e), Ti2p (f) and O1s (g) regions.

3.5 Optical properties

In order to understand the photocatalytic characteristics of the synthesized $BiVO_4/TiO_2$ nanocomposites, it is important to compare some of their particular properties such as reflectance and photoluminescence with those of pure $BiVO_4$ and TiO_2. The ordinary photographs and the UV-Visible absorbance spectra of TiO_2 inverse opal, $BiVO_4$ nanoparticles and two $BiVO_4/TiO_2$ nanocomposites are shown in Fig. 7A and B, respectively. From Fig. 7A titania inverse opal (a) has a white color. Adding bismuth vanadate (d) which has a strong yellow color, the tone of the white changes in two different manners. In the sample with 0.04$BiVO_4$/3DOM TiO_2 (b), the color turns on a light yellow tone. With increasing the amount of $BiVO_4$ to 0.08 (c) the yellow colour becomes more intense. It can be clearly seen that with an increasing amount of $BiVO_4$, the absorption edge of the $BiVO_4$/3DOM TiO_2 nanocomposite is red shifted to longer wavelengths within the visible-light range (spectra b and c of Fig. 6B), with the spectral response range of TiO_2 being extended. $BiVO_4$ nanoparticles sample (spectrum d of Fig. 7B) showed an absorption edge around 527 nm, which could be responsible for any potential visible-light induced photocatalytic activity.

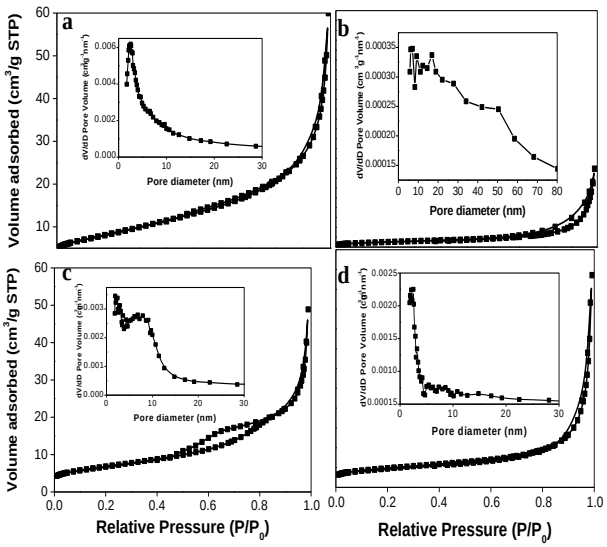

Fig. 6 N_2 adsorption–desorption isotherms and pore size distributions (insets) of the as-synthesized TiO_2 IO (a), $BiVO_4$ nanoparticles (b), 0.04$BiVO_4$/3DOM TiO_2, (c) and 0.08$BiVO_4$/3DOM TiO_2 (d) heterojunction photocatalysts.

Table 1, BET specific surface area, Average pore diameter and pore volume of 3DOM TiO_2 and $BiVO_4$/3DOM TiO_2 heterojunction photocatalysts.

Sample	S_{BET} m^2/g	Pore size/nm	Pore volume cm^3/g
$BiVO_4$	4	23	0.00032
TiO_2	30	2.3	0.0062
0.04 $BiVO_4$/3DOM TiO_2	25	2.4	0.0028
0.08 $BiVO_4$/3DOM TiO_2	17	2.5	0.0022

The steep absorption edge in the visible range indicates that the absorption of visible light is not due to the transition from impurity levels but to the band gap transition, [35,36] originating from charge transfer response of monoclinic $BiVO_4$ from the valence band populated by hybridization of O2p orbital and Bi 6s orbital to the conduction band formed by V3d orbital.[42] As can be shown the absorbance of the $BiVO_4$/3DOM TiO_2 nanocomposites in the visible light region increases with increasing the amount of bismuth vanadate (spectra b, c and d of Fig. 6B). The change in light absorption can be inferred even from the colours of the various compounds.

The band gap energies of the as-prepared samples could thus be estimated from a plot of $(\alpha h\nu)^{1/2}$ versus the photon energy ($h\nu$) via the Kubelka-Munk method:[56-58]

$\alpha h\nu = A\,(h\nu - Eg)^{1/2}$, where α, h, ν, Eg, and A are the absorption coefficient, Planck's constant, light frequency, band gap energy, and a constant, respectively.

The intercept of the tangents to the x-axis gives a good approximation of the band gap energy for the materials. As shown in Fig. 7C, the estimated band gaps of the $BiVO_4$ nanoparticles, TiO_2 inverse opal, 0.04$BiVO_4$/3DOM TiO_2 and 0.08$BiVO_4$/3DOM TiO_2 photocatalysts were about 2.37, 3.15, 2.45 and 2.4 eV, respectively. From these results it can be confirmed that the $BiVO_4$ semiconductor acts as a visible light absorber for TiO_2, leading to effective separation of photoinduced electron–hole pairs, thus reducing the likelihood of recombination. In order to investigate whether thiscould be possible, photoluminescence (PL) measurements were carried out.

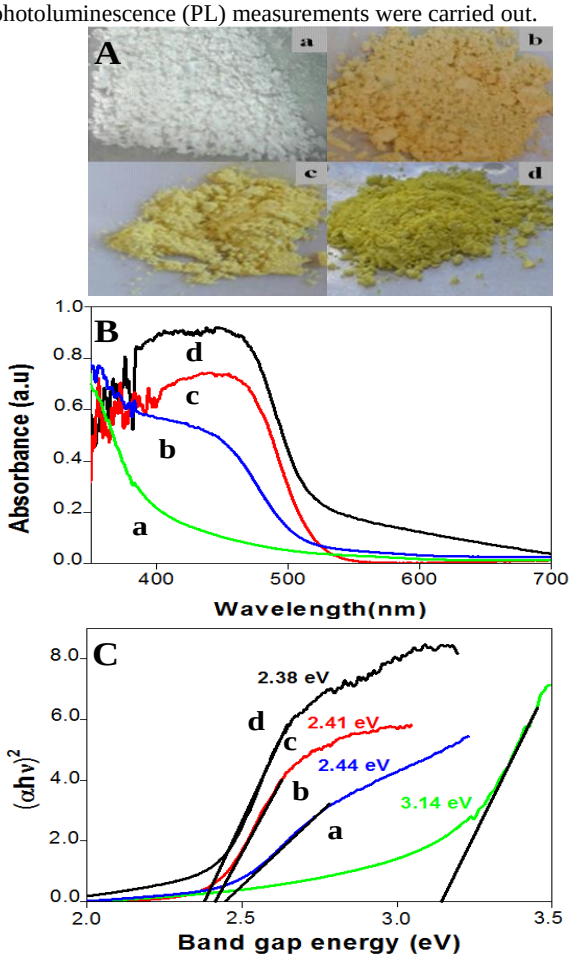

Fig. 7 (A) Ordinary photographs. (B) UV/vis diffuse absorbance spectra., and (C) a plot of$(\alpha h\nu)^{1/2}$versus band gap energy of (a) 3DOM TiO_2,(b) 0.04$BiVO_4$/3DOM TiO_2,(c) 0.08$BiVO_4$/3DOM TiO_2 and (d) $BiVO_4$ photocatalysts.

Fig. 8 shows photoluminescence (PL) emission spectra of pure $BiVO_4$ nanoparticles, pure TiO_2 inverse opal and $BiVO_4$/3DOM TiO_2 nanoheterostructured photocatalysts, which have been used to provide information on the efficiency of charge carrier trapping, migration and transfer.

It is very helpful to understand the fate of the electron-hole pairs in semiconductors as PL emission stems from the recombination of free carriers. The PL intensity depends on the recombination of excited electrons and holes. The lower the PL emission intensity is, the lower the recombination property of the sample is. As can be seen, $BiVO_4$ (spectrum a) exhibits a weak emission at 525 nm which is caused by electron-hole recombination at surface traps. The overall PL emission intensity of $BiVO_4$ is the lowest, indicating very low recombination rate of electron-hole pairs in this material. It can also be observed that the bare TiO_2 (spectrum d) exhibits a strong PL signal in the range 400 to 450 nm, and has four obvious PL peaks at about 442, 460, 493 and 525nm, respectively, possibly the former mainly resulting from band edge free excitons, the latter mainly resulting from binding excitons.[59,60] The overall PL emission intensity of TiO_2 is the highest, showing its highest recombination rate of electron-hole pairs, being unfavourable for photocatalysis. However, the characteristic emission of TiO_2 is significantly affected after introduction of $BiVO_4$ nanoparticles and the intensity is progressively reduced with increasing $BiVO_4$ amount in 3DOM TiO_2 IO structure. This behaviour shows that efficient charge or energy transfer occurs at the $BiVO_4/TiO_2$ heterojunction interface. The observation of PL bands depends on the excitation wavelengths. For example, no PL bands when the excitation wavelength is 320 nm for $BiVO_4$ nanoparticles while some PL bands, in spite of low intensity, are indeed observed with excitation wavelength of 515 nm (Figure 2S). These are due to different electron-hole generation and recombination between different bands (Figure 3S).

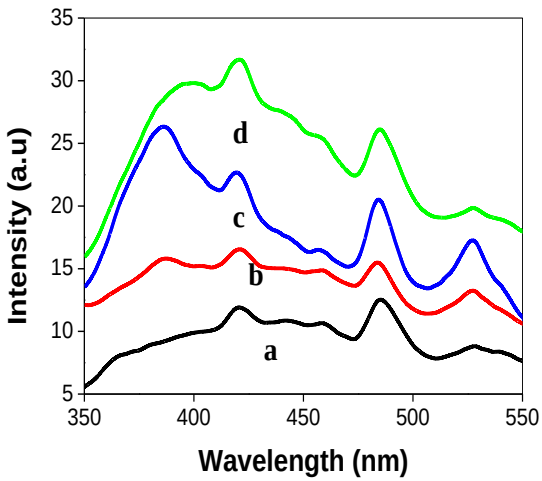

Fig.8 Photoluminescence spectra of (a) pure $BiVO_4$, (b) $0.08BiVO_4/TiO_2$,(c) $0.04BiVO_4/TiO_2$ and (d) pure TiO_2.

According to the positions of the CB and VB of TiO_2 and those of $BiVO_4$ and XPS results, this also suggests that interactions between $BiVO_4$ and TiO_2 involve charge transfer of photoexcited electrons from the conductive band of the donor $BiVO_4$ to empty electronic states of the acceptor TiO_2 and a better charge separation in space in $BiVO_4$/3DOM TiO_2 nanocomposites. These observations are in good agreement with those observed by XPS study. More details will be given in the following sections.

3.6 Photocatlytic activity

The degradation of Rhodamine B (RhB) under visible light irradiation was conducted, as a test reaction, in the presence of each material. The absorption spectrum in the range 500-600 nm for different time intervals for $0.08BiVO_4$/3DOM TiO_2 nanocomposite photocatalyst is shown in Fig. 9A as an example. It has been shown that the major absorption peaks of RhB, located at around 554 nm, diminished gradually under visible light irradiation in the presence of $BiVO_4$/3DOM TiO_2 nanocomposite. The photocatalytic efficiencies (C/C_0) of pure $BiVO_4$ nanoparticles, pure 3DOM TiO_2 inverse opal, two reference samples (phy-Mix 0.08 $BiVO_4$-3DOM TiO_2 IO and 0.08 $BiVO_4$/P25-TiO_2 nanoparticles) and two $BiVO_4/TiO_2$ nanocomposites are illustrated in Fig. 9B. The blank experiment of RhB degradation without the presence of photocatalyst was shown in curve a of Figure 9B. A very low degradation rate of RhB, similar to that reported in literature, was observed and can be neglected. It can clearly be observed that for all samples the degradation of RhB increases gradually with increasing irradiation time. $BiVO_4$ nanoparticles exhibit a very poor photocatalytic activity, with only 22 % of RhB being degraded in 50 min., despite its strong absorption in the visible region. Under the same illumination conditions 28 % of the RhB solution was degraded by 3DOM anatase TiO_2 inverse opal. However due to its wide band gap energy in the UV range, TiO_2 could not absorb in the visible range. Thus theoretically, no possible degradation of dye molecules by TiO_2 can be expected. Its good degradation rate could be resulted from its particular 3DOM IO

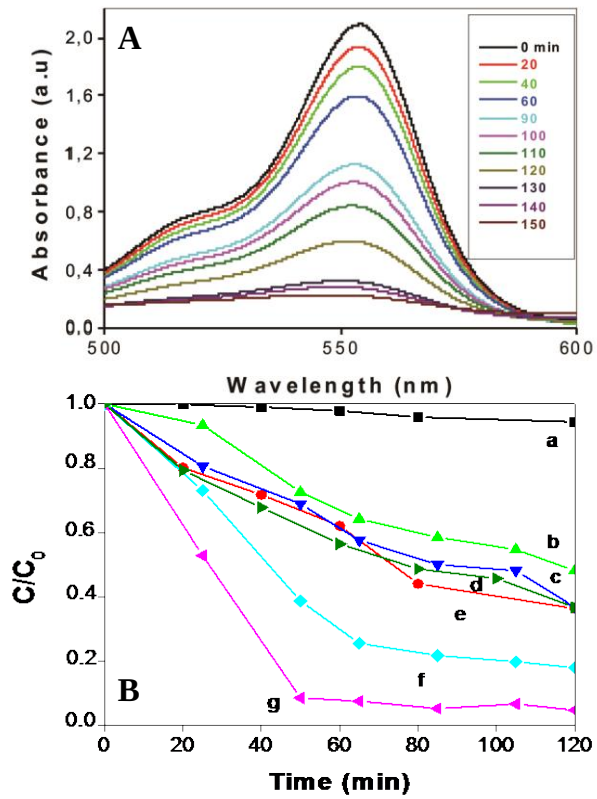

Fig. 9 (A) The temporal evolution of the absorption spectra of the RhB solution in the presence of 0.08 $BiVO_4$/3DOM TiO_2 photocatalysts under visible-light illumination. (B) The variation of RhB concentrations (C/C_0) with irradiation time over different photocatalysts: (a) a blank, (b) $BiVO_4$ nanoparticles, (c) pure 3DOM TiO_2, (d) phy-mix $0.08BiVO_4$-3DOM TiO_2, (e) $0.08BiVO_4$/P25 TiO_2, (f) $0.04BiVO_4$/3DOM TiO_2 and (g) $0.08BiVO_4$/3DOM TiO_2

structure. We will explain this observation in the following paragraph. The photocatalytic performance of TiO_2 can be improved by coupling catalysts with sensitizers leading to the $BiVO_4/TiO_2$ nanocomposite proposed herein with a narrow band gap and thus higher photocatalytic activity. The increase in performance was demonstrated by a superior photodegradation of RhB, with the destruction of 80 % and 95 % RhB over a 120 min period in the presence of $0.04BiVO_4$/3DOM TiO_2 and $0.08BiVO_4$/3DOM TiO_2, respectively.

It has been reported that the photocatalytic degradation process of RhB follows first-order kinetics.[60] The kinetics of RhB degradation with the different samples is illustrated in Fig. 10. The rate constants of the pure $BiVO_4$ nanoparticles, pure TiO_2 inverse opal, phy-mix 0.08 $BiVO_4$-3DOM TiO_2, 0.08 $BiVO_4$/P25-TiO_2, $0.04BiVO_4$/3DOM TiO_2 and $0.08BiVO_4$/3DOM TiO_2 photocatalysts are calculated to be 0.0062, 0.0078, 0.0079, 0.0084, 0.0152 and 0.0256 min^{-1} respectively. From the rate constants (k) in Fig. 10, it can be inferred that the order for the photodegradation rates is: $0.08BiVO_4$/3DOM TiO_2 > $0.04BiVO_4$/3DOM TiO_2 > 0.08 $BiVO_4$/P25-TiO_2 > phy-mix 0.08 $BiVO_4$-3DOM TiO_2 ≥ 3DOM TiO_2 > $BiVO_4$. The nanocomposite of $0.08BiVO_4$/3DOM TiO_2 has a photocatalytic activity 4 times and 3 times higher than pure $BiVO_4$ and 3DOM TiO_2, respectively, showing high impact of $BiVO_4$/3DOM TiO_2 heterojunction on the photocatalytic performance. The reference sample prepared by a physical mixing of $BiVO_4$ and 3DOM TiO_2 IO has the similar photocatalytic activity to that of pure 3DOM TiO_2 IO, indicating that the introduction of low amount of $BiVO_4$ into 3DOM TiO_2 IO by physical mixing does not induce an effect on the photocatalytic activity and the importance of the intimate contact between $BiVO_4$ and 3DOM TiO_2 IO structure. Another reference sample $0.08BiVO_4$/P25-TiO_2 prepared by the same hydrothermal method as $BiVO_4$/3DOM TiO_2 showed a higher photocatalytic activity than that of pure 3DOM TiO_2 and that of the physical mixing sample and pure $BiVO_4$ nanaoparticles, but much lower than that of $BiVO_4$/3DOM TiO_2 nanocomposites, confirming again the enhancement by the intimate contact between $BiVO_4$ and TiO_2 and the importance of 3DOM inverse opal structure.

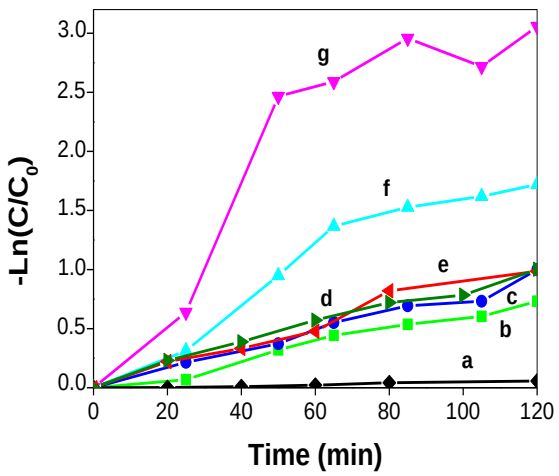

Fig. 10 Kinetics of RhB degradation with (a) a blank, (b) $BiVO_4$ nanoparticles, (c) 3DOM TiO_2, (d) physical mixture of $0.08BiVO_4$-3DOM TiO_2, (e) $0.08BiVO_4$/P25-TiO_2 nanoparticles, (f) $0.04BiVO_4$/3DOM TiO_2 and (g) $0.08BiVO_4$/3DOM TiO_2 nanocomposite photocatalysts.

It is clear that the photocatalytic activity of $BiVO_4/TiO_2$ nanocomposite photocatalysts is strongly dependent on the amount of $BiVO_4$. The photodegradation activity of (x) $BiVO_4$:TiO_2 increases remarkably with an increasing amount of $BiVO_4$ up to x = 0.08. The enhanced photocatalytic activity may originate from the interfacial transfer of electrons and holes as observed by PL and XPS studies. The lifetime of the charge carriers is increased thus the recombination of electron-hole pairs can be inhibited which resulted in an elevation of the photocatalytic efficiency of TiO_2 under visible-light irradiation. As comparison, Cao et al.[24] studied the photocatalytic activity of $BiVO_4/TiO_2$ composite under simulated sun-light irradiation. The photocatalytic activities of the $BiVO_4/TiO_2$ composites with different ratio were evaluated by the degradation of RhB at room temperature. They found that a 20 wt% $TiO_2/BiVO_4$ shows the higher activity with a constant rate equal to 0.04 min^{-1}.

3.7 Photocatalytic mechanism

The coupling of different semiconductor oxides seems useful in order to absorb a wide range of solar radiation and to achieve a more efficient electron–hole pair separation when under irradiation and, consequently, a higher photocatalytic activity. A schematic representation of our $BiVO_4$/3DOM TiO_2 nanocomposites with bismuth vanadate nanoparticles incorporated in 3DOM inverse opal TiO_2 matrix is presented in Fig. 11 A. The combination of $BiVO_4$ and TiO_2 attracted much attention recently in photocatalysis.[20,24-31] However, the photocatalytic promoting mechanism remains unclear and diverging. Hu et al[26] proposed a band configuration where the CB and the VB bands of $BiVO_4$ were positioned at the locations higher than the CB and the VB of pure TiO_2, respectively. Under visible light irradiation, electrons of the VB of $BiVO_4$ are promoted to its CB, leaving holes behind. Electrons at the CB of $BiVO_4$ can now be transferred to the CB of TiO_2. Electrons at the CB of TiO_2 are good reductants which can capture the adsorbed O_2 and reduce it to $O_2^{\cdot-}$ to oxidize dye molecules. The holes at the VB of $BiVO_4$ can react with OH^- to give rise $OH^\cdot$ which can also be used for the degradation of dye molecules. They claimed that $BiVO_4$ played a role of light sensitizer. The photodegradation of organic molecules occurred at the side of $BiVO_4$. However, our present results show that pure $BiVO_4$ gave a very low photocatalytic activity. Different electronic mechanism should be involved. Zheng et al[25] proposed a different electronic mechanism. On the basis of their calculations, they placed the CB and VB of $BiVO_4$ between the CB and the VB of TiO_2. They suggested under both UV and visible light irradiation that the photogenerated electrons from RhB dye molecules are transferred to the CB of TiO_2 which are in turn transferred to the CB of $BiVO_4$, leaving the holes at the VB of TiO_2. They proposed that the reduction of RhB occurs at the CB of $BiVO_4$ and the oxidation of RhB can take place at the VB of both TiO_2 and $BiVO_4$. Colon et al[31] postulated a similar electronic mechanism with the similar positions of the CB and the VB of TiO_2 and those of $BiVO_4$. However, this proposition concerning the positions of the CB and VB of TiO_2 and those of $BiVO_4$ remain to be confirmed. In some very recent papers, the positions of the CB and VB of TiO_2 and $BiVO_4$ were revisited. A generally accepted point is that under visible light irradiation, electrons of the VB of $BiVO_4$ will be firstly excited to the CB of $BiVO_4$, leaving holes behind and these photogenerated electrons will be transferred to the CB of TiO_2. Tang et al[30] pointed out that electrons transfer from $BiVO_4$ to TiO_2 is feasible since E_{cb} of TiO_2 is considered to be located just under the conduction band of $BiVO_4$. Fu et al[29] in their excellent recent paper confirmed this suggestion that electrons are transferred from $BiVO_4$ to TiO_2. $BiVO_4$ can be considered as light sensitizer for TiO_2.

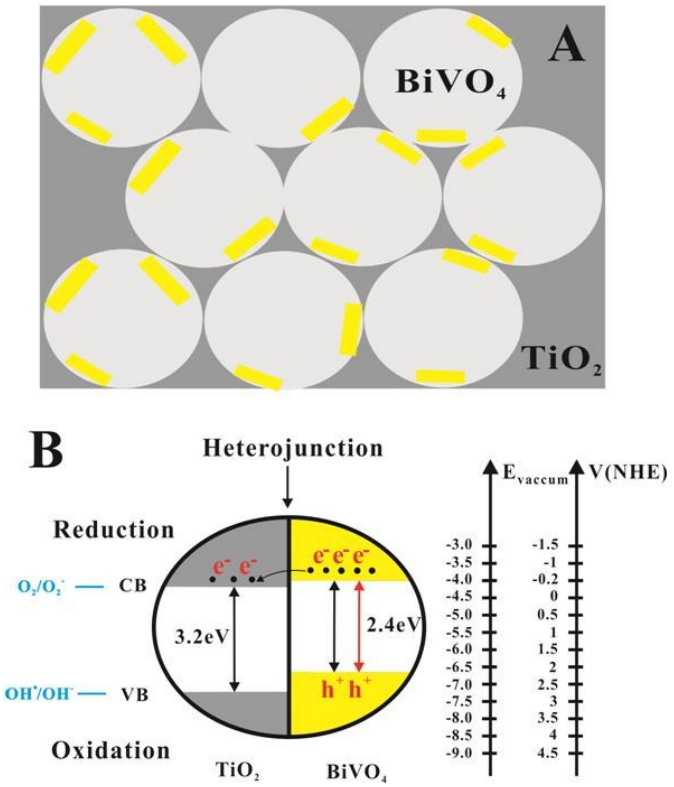

Fig.11 (A) Schematic representation of $BiVO_4/TiO_2$ nanocomposites. (B) Energy band diagram and charge transfer processes in $BiVO_4/TiO_2$ nanostructured photocatalysts under visible light irradiation.

On the basis of the above analysis, our XPS results, photocatalytic performance of a series of materials studied herein and the fact that pure $BiVO_4$ gives an unexpectedly low photocatalytic activity in the degradation of RhB dye molecules, a new energy band diagram of the $BiVO_4/TiO_2$ heterojunction photocatalysts is proposed and presented in Fig. 11 B. It should be taken into account the fact that the work function for RhB is -5.45 eV and -3.08eV for excited RhB.[61] For $BiVO_4$, a valence band (VB) edge potential of 1.90 V (NHE scale) was reported by Su et al.[62] while the VB of TiO_2 was reported as 2.82 V (NHE scale) by Hagfeldt et al.[63] and Sayama et al.[64] The mesured band gap energies of TiO_2 and $BiVO_4$ by the present study were around 3.15 and 2.37 eV, respectively. The position of aconduction band (CB) edge is determined by $E_{CB} = E_{VB} - Eg$. Thus, the calculated CB of $BiVO_4$ and TiO_2 were -0.47 and -0.27 eV, respectively. The difference in the conduction band energies between $BiVO_4$ and TiO_2 allows the transfer of electrons from the conduction band of $BiVO_4$ to that of TiO_2 since the position of the CB of TiO_2 is just under that of $BiVO_4$.

When the system is irradiated with visible light, $BiVO_4$ is activated to generate electron-hole pairs. An electron (e^-) is promoted from the valence band VB into the conduction band CB of $BiVO_4$, leaving a hole (h^+) behind. The excited-state electrons produced by $BiVO_4$ can be injected into the conduction band of the coupled TiO_2 due to the intimate joint of the electric fields between the two materials and the position of the CB of TiO_2 is just under the CB of $BiVO_4$ as indicated by Tang et al.[30] The electron transfer is feasible. The electron and holes are physically separated in space, reducing the opportunity of their recombination. The conduction electrons at TiO_2 side are good reductants which can be scavenged by molecular oxygen O_2 to yield the superoxide radical anion O_2^-. The holes at VB of $BiVO_4$ will interact with hydroxyl groups to form OH · radicals. It is well known that the OH· radical is a powerful oxidizing agent capable of degrading most pollutants. In the present case, RhB dye model molecules will be degraded by O_2^- and OH· radicals. Anatase TiO_2 inverse opal has a too large gap so that no electrons can be promoted from the VB to CB thus no electron-hole pairs can be formed under visible light irradiation.

Concerning pure $BiVO_4$ nanoparticles, the band gap is around 2.4 eV and located in the visible light zone. However, an unexpected low photocatalytic activity towards RhB dye molecules, even lower than that of anatase TiO_2 inverse opal structure has been observed. The same phenomenon that the photocatalytic activity of monoclinic $BiVO_4$ in the degradation of phenol is lower than that of pure anatase TiO_2 in the visible light range has been previously reported by Colon et al[20]. The low photocatalytic activity of single phase of $BiVO_4$ photocatalysts was also pointed out by Fresno et al[27], Li et al[21] and Jiang et al.[33] The lower photocatalytic activity of pure monoclinic $BiVO_4$ compared to 3DOM TiO_2 observed in the present study can be from two different reasons. Firstly, although our PL study showed that pure monoclinic $BiVO_4$ has a very low recombination rate of electron-holes, due to its intrinsic characters of pure $BiVO_4$ as to its very poor adsorptive performance towards organic dye molecules and the inefficient migration of photogenerated electron-hole pairs to surface for photocatalytic reaction, the pure monoclinic $BiVO_4$ presented an unexpectedly low photocatalytic activity in the visible light degradation of organic dye pollutants. [21,33] The combination with TiO_2 can largely improve the adsorption properties and migration rate of electron-hole pairs towards surface of $BiVO_4$/3DOM TiO_2 facilitating the electron transfer from the CB of $BiVO_4$ to the CB of TiO_2. Secondly, as RhB molecules can absorb visible light, it is possible that some electrons can be promoted from HOMO (-5.45 eV) to LUMO (-3.08 eV) and these electrons of RhB can migrate to CB of anatase TiO_2 to generate reactive O_2^- to degrade RhB dye molecules. This is why the degradation of RhB can be observed on anatase TiO_2 inverse opal in the visible light range although TiO_2 absorbs only UV light and the activity is even higher than that of $BiVO_4$ nanoparticles.

It is worthy noting that our 3 DOM TiO_2 presented a very interesting photodegradation activity in visible zone. It is well-known that TiO_2 has a large electronic band gap and can not absorb visible light and should not present a photodegradation activity of dye molecules in visible zone. The dye molecule degradation rate of pure TiO_2 inverse opal has been reported by Lee et al.[65] Their TiO_2 IO sample gave a degradation rate of 5% after 120 minutes, being much lower than the photocatalytic activity observed for our pure TiO_2 inverse opal. The difference is because 1) different preparation conditions: their TiO_2 IO sample was calcined at 850 °C and contained mainly rutile phase, while our sample was calcined at 550 °C and contained only anatase phase. It is well known that the rutile phase is less active than anatase phase. 2) different photocatalytic conditions: in their case, they used Methylene blue while in our case, we used Rh B as reactants; 3) different characteristics of samples: their sample had a macropore size of 500 nm while our sample had a macropore size of 250 nm. Their sample is in a shape of film while our sample is in powder shape. Our sample had a higher surface area, i.e. higher contact area. Due to above reasons, their sample presented different activity compared to our 3DOM TiO_2 powder. However, one point is important to underline that our bare 3DOM TiO_2 IO sample gave an unexpectedly high degradation rate of 28%. The reason is very probably related to the 3DOM TiO_2 IO structure which could generate the slow photon effect so that the photocatalytic activity is enhanced. Ozin's group and our group have reported this effect for TiO_2 IO in

form of films for visible light and UV light in gas phase[47-49] and liquid phase [39,49,50] photocatalytic degradation of dye molecules, respectively. Our present sample could have this slow photon effect to give an enhancement in photocatalytic activity even in the visible light zone, being in a good agreement with the observation made by Ozin et al with similar pore size of TiO_2 IO.[47-49] That is why we observed a degradation activity of 28 % which is not observed for P25 in visible light zone. We are working on this effect to better investigate the slow photon effect in visible light zone to enhance the photocatalytic activity. However, due to its powdery shape, the investigation is much more difficult than film shaped samples. Another point is that the 3DOM TiO_2 can provide more active surface areas, more contact area and increase mass transfer because of its highly accessible 3D porosity. We prepared a reference sample by the deposition of $BiVO_4$ nanoparticles on P25-TiO_2 nanoparticles using the same hydrothermal preparation method. The phtocatalytic activity of 3DOM $BiVO_4/TiO_2$ nanocomposites is much higher than that of $BiVO_4/TiO_2$-P25 nanocomposite, showing very clearly the effect of 3DOM TiO_2 inverse opal structure.

We also performed a control experiment in the photodegradation of RhB using a physical mixture (e.g., grinding) of $BiVO_4$ dumbbell nanoparticles and 3DOM TiO_2 powder and compared its photocatalytic activity with that of $BiVO_4$/3DOM TiO_2 nanocomposite. It is evidenced that the photocatalytic activity of the physical mixture (e.g., grinding) of $BiVO_4$ dumbbell and 3DOM TiO_2 is very similar to that of pure 3DOM TiO_2 inverse opal structure and slightly higher than that of pure $BiVO_4$ dumbbell, but much lower than that of $BiVO_4$/3DOM TiO_2 IO nanocomposites prepared by careful deposition of $BiVO_4$ nanoparticles on 3DOM TiO_2 IO structure to have an intimate contact between two phases, illustrating the advantage of intimate contact between $BiVO_4$ nanoparticles and 3DOM inverse opal structure.

When narrow band gap sensitizer $BiVO_4$ and large band gap photocatalyst TiO_2 are in intimate contact in 3DOM $BiVO_4/TiO_2$ nanocomposite, the draw backs such as the rapid e^-- h^+ recombination occurred in TiO_2, the poor adsorption properties and low migration rate of electron-holes of pure $BiVO_4$ towards its surface and no excitation of TiO_2 in visible light range can be avoided. Under visible light irradiation, the electrons at the CB excited from the VB of $BiVO_4$ can migrate to the CB of TiO_2 photocatalyst to generate very reactive O_2^- species. The h^+ generated at VB of $BiVO_4$ can react with hydroxyl groups to form oxidizing agent OH^-. Both O_2^- and OH^- at the surface of $BiVO_4$/3DOM TiO_2 nanocomposite will degrade RhB dye pollutants adsorbed by TiO_2. $BiVO_4$ in our $BiVO_4$/3DOM TiO_2 nanocomposites play a role of light sensitizer, accelerating the photodegradation rate of RhB by 3DOM TiO_2. More $BiVO_4$, more sensitizing effect, i.e. better light absorption (suggested by diffuse reflectance) and better charge separation effect (suggested by PL). Two effects make 0.08BiVO4/3DOM TiO_2 sample better photocatalyst. However, there exists an optimal amount of $BiVO_4$ amount. We are working to determine this optimal amount. More $BiVO_4$ in TiO_2 inverse opal, more electrons–holes generated in $BiVO_4$/3DOM TiO_2 nanocomposite, higher photocatalytic activity is. It is clear that the 3DOM $BiVO_4/TiO_2$ nanocomposite with intimate contact can be an efficient way to design long-lived visible light excited charge carriers for photocatalysis.

4 Conclusions

Novel 3DOM $BiVO_4/TiO_2$ nanocomposites have been successfully synthesized**.** According to UV−Vis DRS results, the absorption of $BiVO_4/TiO_2$ nanocomposites increased in the visible region. Moreover, the low band gap energy of $BiVO_4/TiO_2$ nanocomposites also influenced dye degradation, and showed significant promise for this nanocomposite to be employed as an effective visible light photocatalyst for dye wastewater treatment, photocatalytic water splitting, CO_2 reduction and other solar applications. In fact, by coupling different band-gap semiconductors such as TiO_2 and $BiVO_4$, the resultant nanocomposites facilitate the separation of the photogenerated carriers under the internal field induced by the different electronic band structures of the semiconductors. Thus the photocatalytic activity of TiO_2 inverse opals was efficiently improved. It can be concluded that adding the narrow band gap energy materials as light sensitizer to TiO_2 is a very promising method to render 3DOM TiO_2 inverse opals more efficient in the photodegradation of organic pollutants and in water splitting reaction under visible light. Thus, compared to 3DOM TiO_2 the 3DOM $BiVO_4/TiO_2$ nanocomposites presented herein exhibit higher photocatalytic activities and can be considered as more efficient as they promote visible- light driven photocatalysis. Increasing $BiVO_4$ amount in nanocomposites can increase the photogenerated charge separation time and in consequence improve again the photocatalytic performance. In the present work, the benefit of 3D porosity and high surface area of TiO_2 inverse opal structure is essential for the accessibility of dye molecules to photocatalysts and for a better dispersion of $BiVO_4$ nanoparticles. However, the benefit of slow photon effect of 3DOM TiO_2 inverse opal photonic crystal structure has not been studied. The future work will focus on the optimisation of the amount of $BiVO_4$ in nanocomposites, the study of other large band gap photocatalyts such as ZnO and taking profit equally the possible slow photon effect of 3DOM TiO_2 inverse opal.

Acknowledgements

This work was realized with the financial support of the Belgian FNRS (Fonds National de la RechercheScientifique). This research used resources of the Electron Microscopy Service located at the University of Namur. This Service is member of the "PlateformeTechnologiqueMorphologie - Imagerie". The XPS analyses were made in the LISE, Department of Physics of University of Namur thanks to Dr. P. Louette. This work was also supported by Changjiang Scholars and Innovative Research Team (IRT1169) of Ministry of Education of the People's Republic of China. B. L. Su acknowledges the Chinese Central Government for an "Expert of the State" position in the Program of the "Thousand Talents" and a Clare Hall Life Membership at the Clare Hall and the financial support of the Department of Chemistry, University of Cambridge.

Notes and references

[a]Laboratory of Inorganic Materials Chemistry (CMI), University of Namur (UNamur), 61 rue de Bruxelles, B-5000 Namur, Belgium. Email: bao-lian.su@unamur.be
[b]Laboratoire de Physique des Matériaux: Structure et Propriétés, Groupe Physique des Composants et Dispositifs Nanométriques, Faculté des Sciences de Bizerte, University of Carthage, 7021 Jarzouna-Bizerte, Tunisia
[c]EMAT (Electron Microscopy for Materials Science), University of Antwerp, Groenenborgerlaan 171,B-2020 Antwerp, Belgium

[d]State Key Laboratory of Advanced Technology for Materials Synthesis and Processing, Wuhan University of Technology, Luoshi Road 122, 430070, Wuhan, Hubei, China. Email: minwu@whut.edu.cn and baoliansu@whut.edu.cn

[e]Department of Chemistryand Clare Hall College, University of Cambridge, Lensfield Road, Cambridge, United Kingdom, Email:bls26@cam.as.uk

+ The authors contribute equally to this work.

1 S. J. Liao, D. G. Huang, D. H. Yu, Y. L. Su and G. Q.Yuan, *J. Photochem. Photobiol*. A, 2004, **168**, 7–13.
2 H. Li, G. Liua and X. Duana, *J. Mater. Chem. Phys*, 2009, **115**, 9-13.
3 W. S. Lu, G. C. Xiao, D. Z. Li, X. Z. Fu and X. X. Wang, Chin. *J.Inorg. Chem*, 2005, **21**, 1495–1499.
4 H. Irie, Y. Watanabe and K. Hashimoto, *J. Phys. Chem*. B, 2003,**107**, 5483–5486.
5 O. Diwald, T.L. Thompson and T. Zubkov, *J. Phys. Chem. B*, **2004**, 108, 6004–6008.
6 N. Serpone, P. Maruthamuthu, P. Pichat, E. Pelizzetti and H. Hidaka, *J. Photochem. Photobiol. A:Chem*,1995,**85**, 247–255.
7 L. M. Peter, D. Jason Riley, E. J. Tull and K. G. UpulWijayantha. *Chem. Commun*, 2002, **10**, 1030–1031.
8 W. Liu, S. F. Chen, S. J. Zhang, W. Zhao, H.Y. Zhang and X. L. Yu, *J. Nanopart. Res*, 2010, **12**, 1355–1366.
9 I. Bedjat and P. Kamat, *J. Phys. Chem*, 1995, **99**, 9182–9188.
10 J. Engweiler, J. Harf and A. Baiker, *J. Catal*, 1996, **159**, 259–269.
11 J. Xu, W. Z. Wang, S. Sun and L. Wang, *Appl. Catal. B*, 2012,**111–112**, 126–132.
12 Y. Liu, F. Xin, F. Wang, S. Luo and X. Yin, *J. Alloys Compd*. **498**, 179–184.
13 E. V. Skorb, E. A. Ustinovich, A. I. Kulak and D. V. Sviridov, *J. Photochem. Photobiol. A* , 2008, **193**, 97–102.
14 L. Huang, F. Peng, H. J. Wang, H. Yu and Z. Li, Catal. *Commun*, 2009, **10**, 1839–1843.
15 Z. D. Meng, L. Zhu, J. G. Choi, C. Y. Park and W. C. Oh, *Nanoscale Res. Lett*, 2011, **6**, 459–469.
16 D. N. Ke, H. J. Liu, T.Y. Peng, X. Liu and K. Dai, *Materials Letters*, 2008, **62**, 447–450.
17 K. Vinodgopal and P.V. Kamat, *Environmental Science and Technology*, 1995, **29**, 841–845.
18 Y. Bessekhouad, D. Robert and V. Weber, *Catalysis Today*, 2005, **101**,315–321.
19 A. Zhang and J. Zhang, *Mater. Lett*., 2009, **63**, 1939–1942.
20 S. Obregon, S. W. Lee and G. Colon, *Dalton Trans.*2014, **43**, 311-316.
21 Y. K. Li, J. Y. Dong, Y. F. Wang, J. Y. Sun, Y. F. Li, Y and Q. Pi, *J. Mol. Catal., A. Chem.* 2014, **387**, 138-146.
22 K. Sayama, A. Nomura, T. Arai, T. Sugita, R. Abe, M. Yanagida, T. Oi, Y. Iwasaki, Y. Abe, H. Sugihara, *J. Phys. Chem. B*, 2006, **110**, 11352-11360.
23 A. Kudo, K. Ueda, H. Kato and I. Mikami, *Catal. Lett*., 1998, **53**, 229–230.
24 B. Cao, J. Peng and Y. Y, *J. Clust. Sci*., 2013, **24**, 771–785.
25 L. Zhang, G. Tan, S. Wei, H. Ren, A. Xia and Y. Luo, *J. Ceram.Int.*, 2013, **39**, 8597–8604.
26 Y. Hu, D. Li, Y. Zheng, W. Chen, Y. He, Y. Shao, X. Fu and G. Xiao, *Appl. Catal. B*, 2011, **104**, 30-36.
27 G. Long, F. Fresno, S. Grosss and U. L. Stangar, *Enriron. Sci. Pollut. Res. Int.* 2014, **21**, 11189-11197.
28 R. Rahimi, S. Zargari and M. M. Moghaddas, *Adv. Mater. Res.* 2013, **702**, 172-175.
29 M. Xie, X. Fu, L. Jing, P. Luan, Y. Feng, H. Fu, *Adv. Energy Mater.* 2014, **4**, 130095.
30 S. Ho-Kimur, S. J. A. Moniz, A. D. Handoko and J. W. Tang, *J. Mater. Chem. A*, 2014, **2**, 3948-3953.
31 S. Obregon and G. Colon, *RSC Adv.*, 2014, **4**, 6820-6926.
32 T. Y. Huo, X. F. Zhang, X. Dong, X. X Zhang, C. Ma, G. W. wang, H. C. Ma, M. Xue, *J. Mater. Chem.* A, 2014, **2**, 17366-17370
33 H. Q. Jiang, H. Endo, H. Natori, M. Nagai and K. Kobayashi, *Mater. Res. Bull.*, 2009, **44**, 700-706.
34 M. Zhou, J. Bao, Y. Xu, J. J. Zhang, J. F. Xie, M. L. Guan, C. L. Wang, L. Y. Web, Y. Lei and Y. Xie, *ACS Nano*, 2014, **8**, 7088-7098
35 M. Wu, Y. Li, Z. Deng and B. L. Su, *ChemSusChem*, 2011, **4**, 1481.
36 X. Zheng, S. Meng, J. Chen, J. Wang, J. Xian, Y. Shao, X. Fu and D. Li, *J. Phys. Chem. C*, 2013, **177**, 21263–21273.
37 C. W. Cheng, S. K. Karuturi, L. J. Liu, J. P. Liu, H. X. Li, L.T. Su, A. I.Y. Tok and H. J. Fan, *Small*., 2012, **8**, 37–42.
38 J. Liu, Y. Li, H. W. Huang, C. Wang, M. Wu, L. H. Chen and B. L. Su, *J. Mater. Chem. A*, 2014, **2**, 5051.
39 M. Wu, J. Jing, J. Liu, Z. Deng, Y. Li, O. Deparis and B. L. Su, *J. Mater. Chem. A*, 2013, **1**, 15491.
40 M. Wu, J. Liu, J. Jing, C. Wang, S. Z. Huang, Z. Deng, Y. Li and B. L. Su, *Appl. Catal, B-Environ*, 2014, **411**, 150–151.
41 X. Chen, J. Ye, S. Ouyang, T. Kako, Z. Li and Z. Zou, *J. Am. Chem. Soc*., 2011, **5**, 4310–4318
42 L. I. Halaoui, N. M. Abrams and T. E. Mallouk, *J. Phys. Chem. B*, 2005, **109**, 6334–6342.
43 P. R. Somani, C. Dionigi, M. Murgia, D. Palles, P. Nozar and G. Ruani, *Sol. Energy Mater. Sol. Cells*, 2005, **87**, 513–519.
44 C. L. Huisman, J. Schoonmanand A. Goossens, *Sol. Energy Mater. Sol. Cells*, 2005, **85**, 115–124.
45 I. Rodriguez, F. Ramiro-Manzano, P. Atienzar, J. M. Martinez, F. Meseguer, H. Garcia and A. Corma, *J. Mater. Chem*., 2007, **17**, 3205–3209.
46 S. Nishimura, N. Abrams, B. A. Lewis, L. I. Halaoui, T. E. Mallouk, K. D. Benkstein, J. Van De Lagemaat and A. Frank, *J.Am. Chem. Soc*., 2003, **125**, 6306–6310.
47 J. I. L. Chen, E. Loso, N. Ebrahim and G. A. Ozin, *J. Am. Chem. Soc.*, 2008, **130**, 5420-5421.
48 J. I. L. Chen, G. von Freymann, S.Y. Choi, V. Kitaev and G.A. Ozin, *Adv. Mater*., 2006, **18**,1915–1919.
49 J. I .L. Chen, G. von Freymann, V. Kitaev and G. A. Ozin, *J. Am. Chem*. Soc., 2007, **129**, 1196–1202.
50 M. Wu, A. Zheng, F. Deng, B. L. Su, *Appl. Catal. B: Environ*, 2013, **138– 139**, 219– 228
51 L. Dong, S. Guo, S. Zhu, D. Xu, L. Zhang, M. Huo and X. Yang, *Catal. Commun*., 2011, **16**, 250–254.
52 Y. Guo, X. Yang, F. Ma, K. Li, L. Xu, X. Yuan and Y. Guo, *Appl. Surf. Sci*., 2010, **256**, 2215–2222.
53 N. Myung, S. Ham, S. Choi, Y. Chae, W. Kim, Y. J. Jeon, K. Paeng, W. Chanmanee, N. R. de Tacconi and K. Rajeshwar, *J. Phys. Chem. C*, 2011, **115**, 7793–7800.
54 Z. Ozlem Kocabaş-Ataklı and Y. Yurum, *J. Chem. Eng*., 2013, **225**, 625-635.
55 Z. F. Bian, J. Zhu, S. H. Wang, Y. Cao, X. F. Qian and H. X. Li, *J. Phys. Chem. C*, 2008, **112**, 6258–6262.
56 Y. Q. Wu, G. X. Lu and S. B. Li, *J. Phys. Chem. C*, 2009, **113**, 9950–9955.
57 A. Zhang and J. Zhang, Mater. Lett., 2009, **63**, 1939–1942.
58 L. D. Zhang and C. M. Mo, *Nanostruct. Mater*., 1995, **6**, 831–834.

59 L. Q. Jing, X. J. Sun, B. F. Xin, B. Q. Wang, W. M. Cai and H. G. Fu, *J. Solid State Chem*., 2004, **177**, 3375–3382.
60 J. Cao, B. Luo, H. Lin, B. Xu, S. Chen, *Appl. Catal. B: Environ*, 2012, **111–112**, 288–296.
61 Z. Xiong, L. L. Zhang, J. Ma and X. S. Zhao, *Chem. Commun*., 2010, **46**, 6011–6099.
62 J. Su, L. Guo, N. Bao and C.A. Grimes, *Nano Lett*., 2011, **11**, 1928–1933.
63 A. Hagfeldt and M. Gratzel, *Chem. Rev*., 1995, **95**, 49–68.
64 K. Sayama, A. Nomura, T. Arai, T. Sugita, R. Abe, M. Yanagida, T. Oi, Y. Iwasaki, Y. Abe and H. Sugihara, *J. Phys. Chem. B*, 2006, **110**, 11352–11360.
65 S. Lee, Y. Lee, D. H. Kim and J. H. Moon, *ACS Appl. Mater. Interfaces*, 2013, **5**, 12526–12532

Novel 3DOM $BiVO_4/TiO_2$ Nanocomposites for Highly Enhanced Photocatalytic Activity

$BiVO_4$ nanoparticles in 3DOM TiO_2 inverse opal structure act as a sensitizer to absorb visible light and to transfer efficiently high energy electrons to TiO_2 to keep photogenerated charges long life and well separated, explaining the extraordinarily high photocatalytic performance of 3DOM $BiVO_4/TiO_2$ nanocomposites.